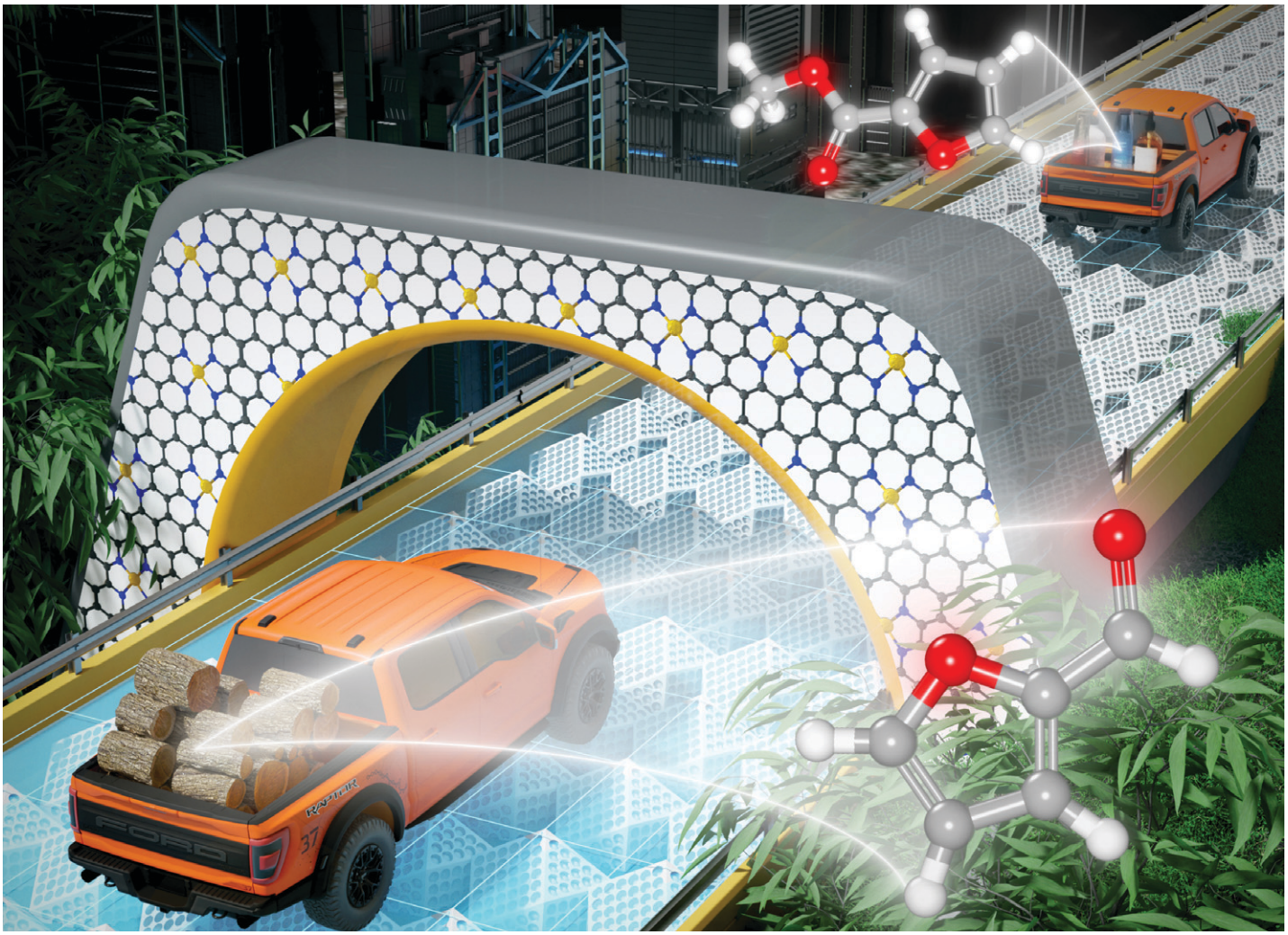

Showcasing research from Yingwei Li's laboratory, School of Chemistry and Chemical Engineering, South China University of Technology, Guangzhou, China.

Hierarchically ordered porous carbon with atomically dispersed cobalt for oxidative esterification of furfural

Co-SA/3DOM-NC catalysts with a three-dimensional ordered macropore structure and highly dispersed CoN4 sites are successfully fabricated, and show high catalytic activity and selectivity in the oxidative esterification of furfural.

As featured in:

See Liyu Chen, Yingwei Li *et al.*, *Ind. Chem. Mater.*, 2023, **1**, 106.

ROYAL SOCIETY OF CHEMISTRY

Industrial Chemistry & Materials

Industrial Chemistry & Materials

ROYAL SOCIETY OF CHEMISTRY

PAPER

View Article Online
View Journal | View Issue

Cite this: *Ind. Chem. Mater.*, 2023, **1**, 106

Hierarchically ordered porous carbon with atomically dispersed cobalt for oxidative esterification of furfural†

Wen Yao,[a] Chenghong Hu,[a] Yajie Zhang,[b] Hao Li,[a] Fengliang Wang,[a] Kui Shen,[a] Liyu Chen *[a] and Yingwei Li *[a]

Received 14th November 2022,
Accepted 19th December 2022

DOI: 10.1039/d2im00045h

rsc.li/icm

Nitrogen-rich zeolitic imidazolate frameworks (ZIFs) are ideal precursors for the synthesis of metal single atoms anchored on N-doped carbon. However, the microporous structures of conventional ZIFs lead to low mass transfer efficiency and low metal utilization of their derivatives. Here, we construct a composite of Co single atoms anchored on nitrogen-doped carbon with a three-dimensional ordered macroporous structure (Co-SA/3DOM-NC) by two-step pyrolysis of ordered macro/microporous ZnCo-ZIF. Co-SA/3DOM-NC shows high activity in the oxidative esterification of furfural, achieving a 99% yield of methyl 2-furoate under mild reaction conditions, which is significantly superior to the microporous and the Co-nanoparticle counterparts. The high activity of Co-SA/3DOM-NC should be attributed to the CoN_4 centers with high intrinsic activity and the ordered macroporous structure, promoting the mass transfer of reactants and accessibility of active sites.

Keywords: Heterogeneous catalysis; Hierarchical pores; Ordered macropore; Oxidative esterification reaction; Single-atom catalysts.

1 Introduction

Renewable biomass resources are promising alternatives for the sustainable supply of chemical intermediates and liquid fuels.[1–4] Furfural (FFA) is one of the key platform chemicals derived from lignocellulosic biomass, with an annual production volume of more than 200 000 tons.[5] The utilization of furfural as a starting material *via* hydrogenation, oxidation, reductive amination, *etc.*, can synthesize a variety of valuable chemicals.[5–8] In particular, the oxidative esterification of furfural can produce alkyl furoates, which are widely used as flavour and fragrance components in the chemical industry. Precious metal-based catalysts show high activity for the oxidative esterification of furfural, while the scarcity of precious metals is unfavourable for industrial applications.[9–13] Therefore, the development of efficient noble metal-free catalysts is highly desired for the transformation of furfural.

Transition-metal single-atom catalysts (SACs) with maximum atomic utilization have been widely used in the fields of catalysis and energy.[14–17] Metal–organic frameworks (MOFs) with porous structures and good designability can serve as a good platform for the synthesis of SACs.[18–28] In particular, N-rich zeolitic imidazolate frameworks (ZIFs) have been utilized as ideal precursors for the fabrication of SACs with catalytically active MN_x centers.[29–37] However, the microporous nature of most ZIFs results in derived SACs with low porosity, which would greatly hinder the mass transfer of reactants and the accessibility of active sites. Recently, we reported a three-dimensional (3D) ordered macroporous ZIF-8 single crystal (SOM-ZIF-8),[38] which can serve as an ideal template/precursor for the construction of SACs with a 3D-ordered macroporous (3DOM) structure.[39–43] The afforded 3DOM-SACs exhibit enhanced performance than their microporous counterparts in the electro/photocatalytic transformations of small molecules (*e.g.*, CO_2, H_2O, O_2).[43–46] However, the application of SOM-MOF-derived SACs in biomass upgrading remains to be explored.

In this work, Co single atoms anchored on 3DOM nitrogen-doped carbon (Co-SA/3DOM-NC) were successfully fabricated by pyrolysis of a bimetallic SOM-ZnCo-ZIF for the oxidative esterification of FFA. Co-SA/3DOM-NC possesses homogeneously distributed single atomic Co sites and interconnected ordered macropores with a diameter of *ca.*

[a] *School of Chemistry and Chemical Engineering, South China University of Technology, Guangzhou 510640, P.R. China. E-mail: liyuchen@scut.edu.cn, liyw@scut.edu.cn*
[b] *State Key Laboratory of Applied Organic Chemistry and Electron Microscopy Centre of Lanzhou University, Lanzhou University, Lanzhou, 730000, P.R. China*

† Electronic supplementary information (ESI) available: Chemicals, preparation, characterization, and performance comparison. See DOI: https://doi.org/10.1039/d2im00045h

150 nm. Co-SA/3DOM-NC shows high catalytic activity in the oxidative esterification of FFA, achieving a 99% conversion of FFA in 6 h at 60 °C, which is much superior to the microporous and Co-nanoparticle counterparts. Moreover, Co-SA/3DOM-NC exhibits high stability, without an apparent decrease of activity even after six runs. Experimental results demonstrate that the CoN_4 centers have high intrinsic activity and the 3D-ordered macroporous structure can effectively promote the mass transfer of reactants and the accessibility of monodispersed Co atoms, leading to the high catalytic performance of Co-SA/3DOM-NC.

2 Results and discussion

The preparation procedure of Co-SA/3DOM-NC is shown in Fig. 1. First, homogeneously dispersed polystyrene spheres (PSs) were synthesized by emulsifier polymerization in an aqueous solution, followed by assembly into 3D-PS monoliths by filtration.[47] The field-emission scanning electron microscopy (SEM) image of the 3D-PS monoliths (Fig. S1†) displays that the PSs are arranged in an order manner with a uniform diameter of ~210 nm. Then, the 3D-PS monoliths were dispersed in the methanol solution of $Co(NO_3)_2$, $Zn(NO_3)_2$, and 2-methylimidazole, followed by soaking in ammonia/methanol solutions to obtain ZnCo-ZIF@PS. Powder X-ray diffraction (XRD) patterns of ZnCo-ZIF@PS are consistent with those of conventional ZIF-8 (Fig. S2†), indicating the formation of ZnCo-ZIF in the voids of the 3D-PS template. Finally, ZnCo-ZIF@PS was pyrolyzed at 400 °C to remove the PS template, followed by carbonization at 920 °C to yield Co-SA/3DOM-NC.

The SEM images show that Co-SA/3DOM-NC possesses a uniform tetrakaidecahedron morphology with a size of 2–3 μm (Fig. 2a–c). The transmission electron microscopy (TEM) images of Co-SA/3DOM-NC display an interconnected ordered macropore structure with a diameter of *ca.* 150 nm and a pore wall thickness of about 20 nm (Fig. 2d and e). In addition, no obvious Co nanoparticles can be observed from the TEM images of Co-SA/3DOM-NC (Fig. 2d), implying that Co species do not agglomerate in the pyrolysis process and are well dispersed in the carbon supports. The aberration-corrected high-angle annular dark-field scanning transmission electron microscopy (HAADF-STEM) image (Fig. 2f) shows well dispersed bright spots on the carbon skeleton, suggesting the existence of Co single atoms.[48] The HAADF-STEM and the corresponding X-ray energy dispersive spectroscopy (EDS) elemental mapping images (Fig. 2g) reveal that Co, N, and C elements are uniformly dispersed in the 3D-ordered macroporous skeleton. The content of Co in Co-SA/3DOM-NC is measured to be 1.7 wt% by atomic absorption spectrometry (AAS) (Table S1†). In addition, there are some residual Zn species in Co-SA/3DOM-NC. Considering that the Zn species show negligible catalytic activity for the oxidative esterification reaction (as shown below), Zn is omitted in the name of the catalysts for the sake of simplification.

The XRD pattern of Co-SA/3DOM-NC displays two broad peaks at ~26° and ~44°, which can be indexed to the (002) and (101) faces of carbon, respectively (Fig. 3a). The Raman spectrum of Co-SA/3DOM-NC shows two vibration peaks appearing at 1350 and 1595 cm^{-1} (Fig. 3b), corresponding to the D band (amorphous carbon) and G band (graphite-type carbon) of carbon, respectively. The I_D/I_G of the Co-SA/3DOM-NC sample is calculated to be 0.99, suggesting the formation of large carbon defects due to N doping.[49–52] The N_2 adsorption–desorption isotherm of Co-SA/3DOM-NC (Fig. 3c) displays a sharp rise stage at low pressures ($P/P_0 < 0.05$) and an obvious hysteresis loop at high pressures, indicating the co-existence of micropores and mesopores.[53] The pore-size distribution indicates that the sizes of the micropores and mesopores are mainly concentrated at 0.6 and 27.5 nm, respectively (Fig. S3†). The Brunauer–Emmett–Teller specific surface area of Co-SA/3DOM-NC is calculated to be 708.6 $m^2\ g^{-1}$ (Table S1†). The interconnected micropore–mesopore–macropore structures are expected to promote the mass transfer of reactants and improve the accessibility of active sites in Co-SA/3DOM-NC.[54]

The electronic structure and chemical environment of Co-SA/3DOM-NC were investigated by X-ray photoelectron spectroscopy (XPS). XPS survey spectra reveal the presence of C, N, and Co in Co-SA/3DOM-NC (Fig. S4†). The high-resolution Co 2p XPS spectrum of Co-SA/3DOM-NC shows a

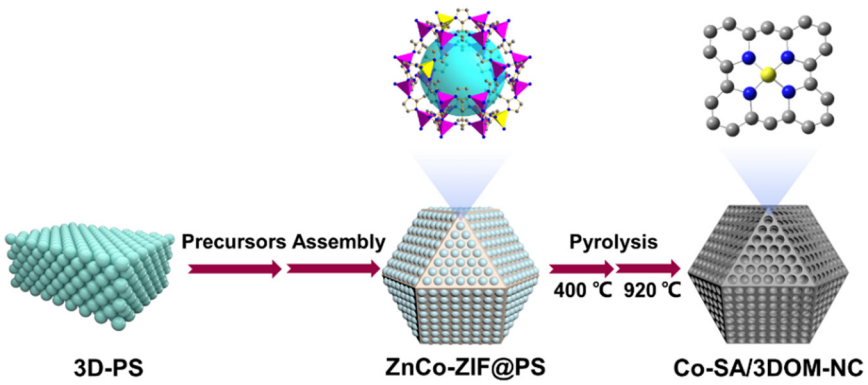

Fig. 1 Schematic illustration of the fabrication of Co-SA/3DOM-NC.

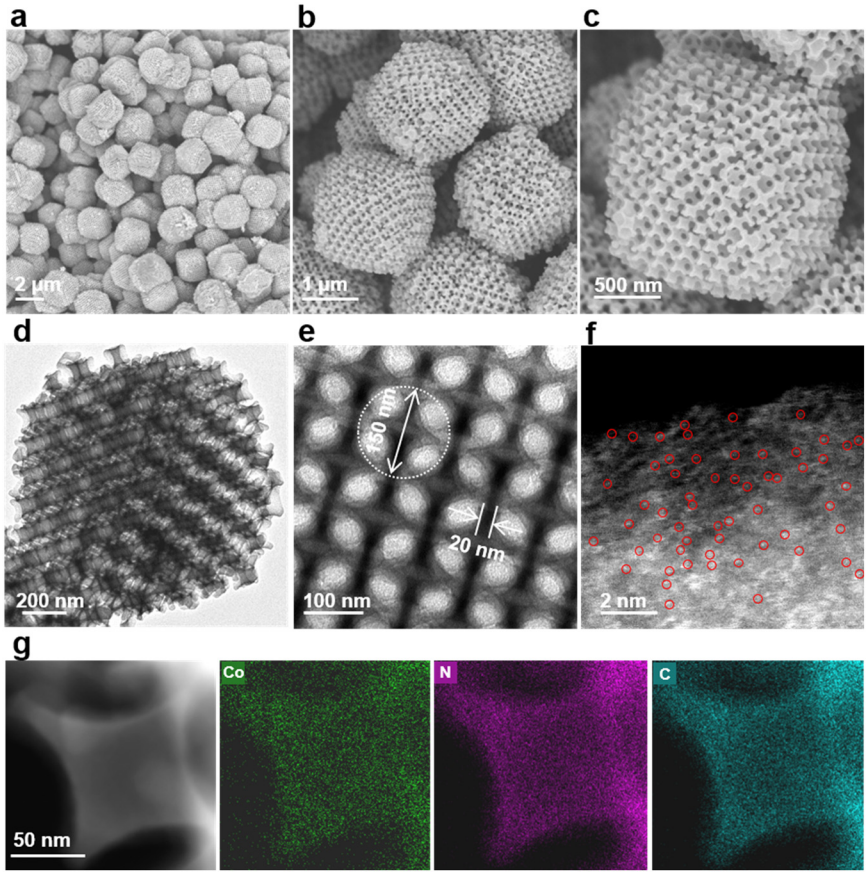

Fig. 2 (a–c) SEM images of Co-SA/3DOM-NC at different magnifications. (d and e) TEM images of Co-SA/3DOM-NC. (f) Aberration-corrected HAADF-STEM image of Co-SA/3DOM-NC. The single atoms are marked with red circles. (g) HAADF-STEM and EDS elemental mapping images of Co-SA/3DOM-NC.

binding energy of Co $2p_{3/2}$ at ~780.9 eV (Fig. 3d), which is between those of Co^{2+} (782.0 eV) and Co^{3+} (780.1 eV). Therefore, the valence state of the Co atom in Co-SA/3DOM-NC is between +2 and +3.[55] High-resolution N 1s XPS spectra can be deconvoluted into four characteristic peaks at 398.7, 399.7, 401.0, and 401.8 eV (Fig. S5†), which may be assigned to pyridinic N, pyrrolic N, graphite-N, and oxidized N, respectively.[56,57]

X-ray absorption fine structure (XAFS) measurements were performed to verify the electronic and geometric structure of Co in Co-SA/3DOM-NC. As shown in the X-ray absorption near-edge structure (XANES) spectra (Fig. 4a), the position of the absorption edge of Co-SA/3DOM-NC is located between those of CoO and Co_3O_4, indicating that the valence state of Co in Co-SA/3DOM-NC is situated between +2 and +3,[58] which is consistent with the XPS results. The Fourier transform extended X-ray absorption fine structure (EXAFS) spectrum of Co-SA/3DOM-NC exhibits a main peak at 1.43 Å (Fig. 4b), corresponding to Co–N coordination. No apparent Co–Co peak at 2.17 Å is detected in Co-SA/3DOM-NC, excluding the formation of Co aggregates. Moreover, the wavelet transform (WT) contour plot of Co in Co-SA/3DOM-NC displays the maximum intensity at 4.5 $Å^{-1}$, assigned to Co–N coordination (Fig. 4d–f). The fitting results further give a coordination number of 3.9 with a bond length of ~1.95 Å for Co–N coordination (Table S2†), inferring that Co atoms in Co-SA/3DOM-NC are coordinated to four N atoms to form the CoN_4 sites (Fig. 4c and S6†).

To verify the role of the 3DOM structure of Co-SA/3DOM-NC, a composite of Co single atoms anchored on a microporous carbon support was prepared, denoted Co-SA/NC. Co-SA/NC was prepared using conventional ZnCo-ZIF as a precursor (Fig. S7†). Co-SA/NC displays a solid microporous structure as observed from the SEM image (Fig. 5a and b). The TEM image of Co-SA/NC shows no Co aggregates on the microporous carbon support (Fig. 5c and d). The XRD pattern of Co-SA/NC only displays peaks assigned to carbon without Co aggregates (Fig. 3a). The HAADF-STEM and corresponding EDS elemental mapping images of Co-SA/NC indicate that Co, N, and C elements are evenly dispersed in the skeleton (Fig. 5e and f). The selected-area electron diffraction (SAED) image (inset of Fig. 5d) shows diffraction rings assigned to graphite carbon without metallic Co. The Raman spectrum of Co-SA/NC exhibits a similar carbon structure to that of Co-SA/3DOM-NC (Fig. 3b). The N_2 sorption isotherm of Co-SA/NC displays a micropore-dominated structure (Fig. 3c and S3†). The Co 2p XPS spectrum of Co-SA/NC shows a

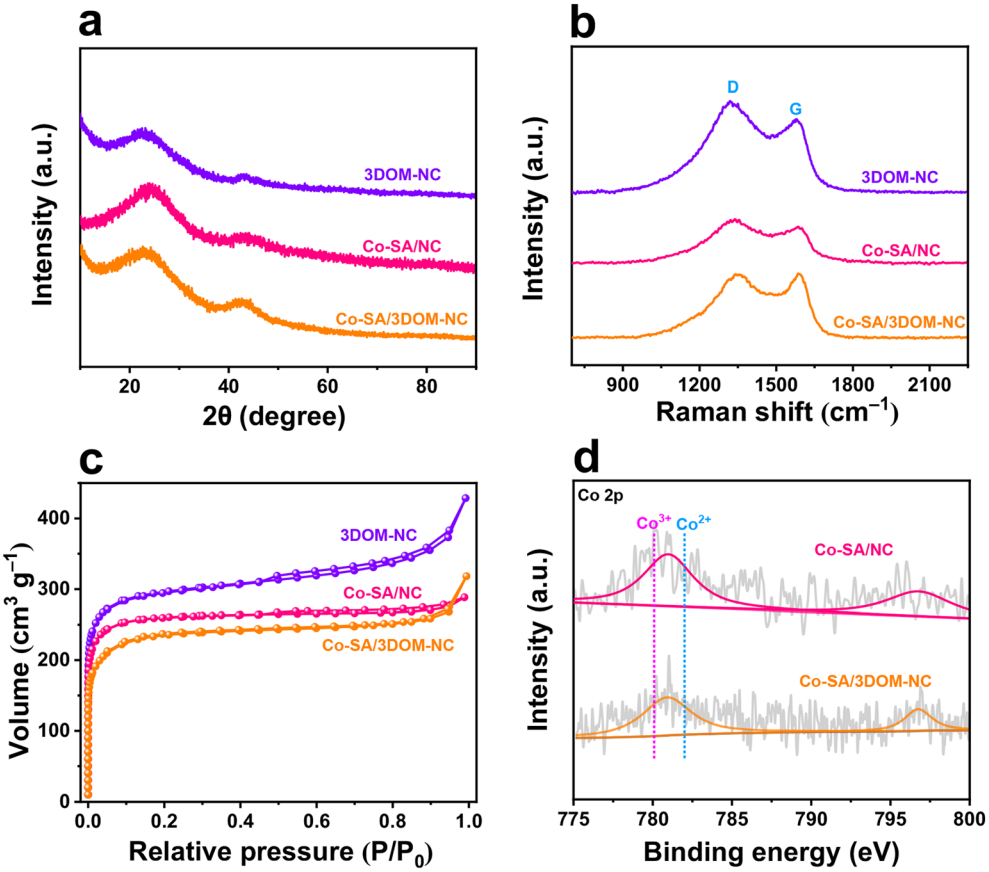

Fig. 3 (a) XRD patterns, (b) Raman spectra, and (c) N_2 adsorption–desorption isotherms of Co-SA/3DOM-NC, Co-SA/NC, and 3DOM-NC. (d) High-resolution Co 2p XPS spectra of Co-SA/3DOM-NC and Co-SA/NC.

similar binding energy to that of Co-SA/3DOM-NC (Fig. 3d), implying their similar electronic structures. The Co of Co-SA/NC was measured to be 1.6 wt% by AAS (Table S1†). In addition, Co-free nitrogen-doped carbon with a 3DOM structure was also synthesized using SOM-ZIF-8 as a precursor, denoted 3DOM-NC. SEM and TEM images display a highly ordered macropore arrangement in 3DOM-NC, similar to Co-SA/3DOM-NC (Fig. 5g–j). The HAADF-STEM and corresponding EDS elemental mapping images of 3DOM-NC reveal that N and C elements are evenly dispersed in the 3DOM skeleton without Co (Fig. 5k and l and S8†). The SAED image (inset of Fig. 5j) of 3DOM-NC shows diffraction rings assigned to graphite carbon. The N_2 sorption isotherm of Co-SA/NC displays typical features of hierarchically porous structures, similar to those of Co-SA/3DOM-NC (Fig. 3c and S3†).

The catalytic performance of Co-SA/3DOM-NC was evaluated in the oxidative esterification of FFA with methanol to methyl 2-furoate (MF) under atmospheric pressure of oxygen (Fig. 6a). The reaction cannot proceed without catalysts. Considering that the stirring speed is an important factor for the external mass transfer of liquid-phase reactions over heterogeneous catalysts, the oxidative esterification reaction over Co-SA/3DOM-NC at different stirring rates was investigated (Table S3†). The conversion of FFA increased from 300 to 500 r min^{-1} and showed no apparent changes with further increase in stirring speed. The catalytic reactions were then carried out at a stirring rate of 700 r min^{-1}, which is sufficiently high for a negligible external mass transfer effect. Co-SA/3DOM-NC exhibits high activity, achieving 99% conversion of FFA in 6 h at 60 °C (Fig. 6b). The decrease in reaction temperature results in a drop in FFA conversion (Fig. 6c). It is worth noting that the performance of Co-SA/3DOM-NC is comparable to the state-of-art catalysts in terms of reaction conditions and catalytic activity (Table S4†). The solid Co-SA/3DOM-NC catalyst was removed from the reaction system at 1 h, and the residue solution was allowed to react for another 11 h. No further reactivity was observed under similar reaction conditions (Fig. 6c), suggesting that the catalytic reaction mainly occurred at the heterogeneous interface.

To reveal the origin of the high activity of Co-SA/3DOM-NC, a variety of comparison materials were prepared and their catalytic activities were evaluated under similar reaction conditions (Fig. 6d and Table S5†). Solid Co-SA/NC only shows a conversion of 18%, much lower than that of Co-SA/3DOM-NC. The TOF values of Co-SA/3DOM-NC and Co-SA/NC based on the total number of Co sites are calculated to be 5.7 and 1.0 h^{-1}, respectively. Considering that solid Co-SA/NC possesses the same CoN_4 centers and

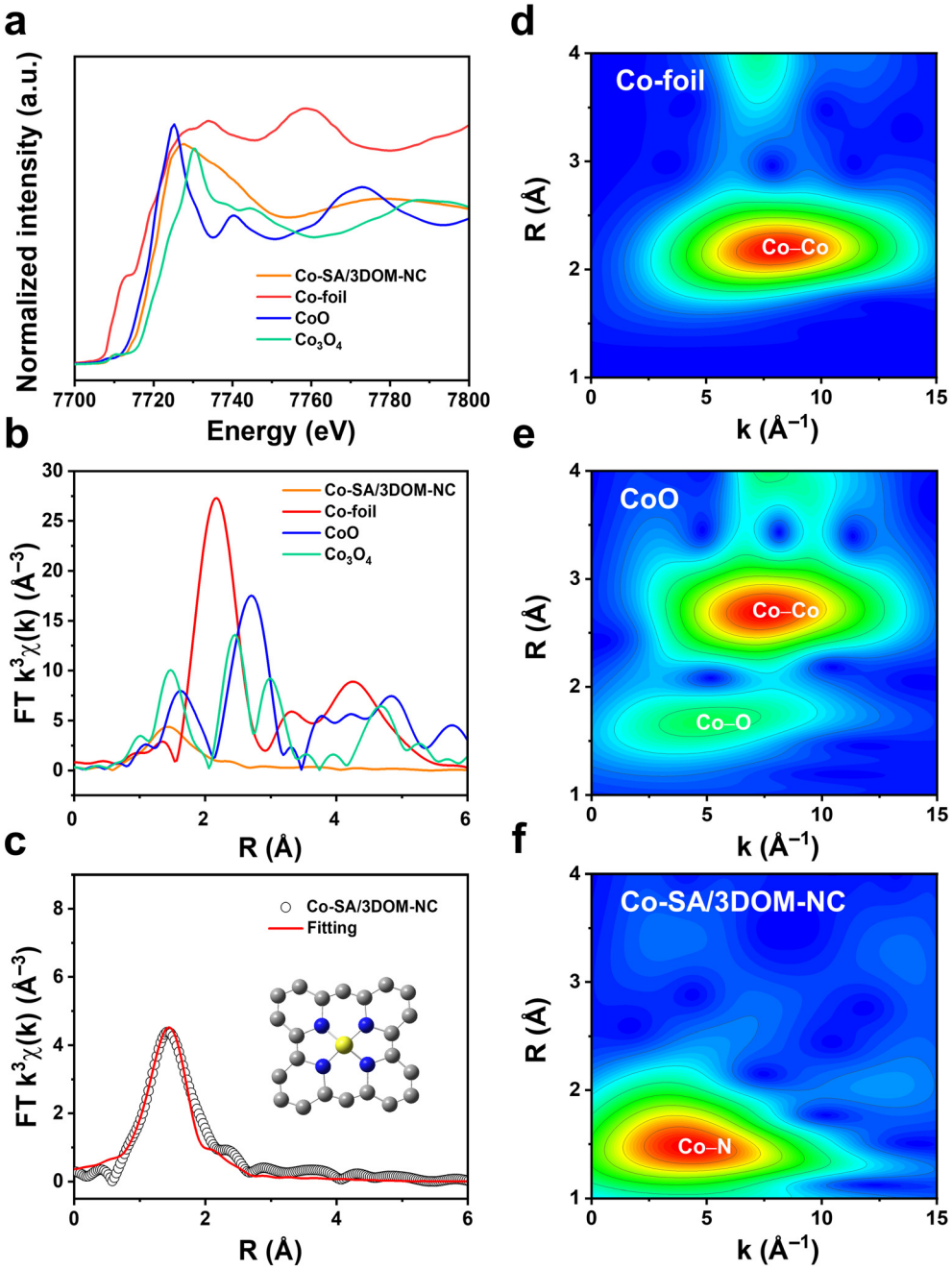

Fig. 4 (a) XANES spectra and (b) Fourier-transform EXAFS spectra of Co-SA/3DOM-NC, Co foil, CoO, and Co_3O_4. (c) Fourier-transform EXAFS fitting curves of Co K-edge for Co-SA/3DOM-NC (inset: a proposed structural model of Co-SA/3DOM-NC). Wavelet-transformed contour plots of Co in (d) Co foil, (e) CoO, and (f) Co-SA/3DOM-NC.

Co loading as Co-SA/3DOM-NC, the calculated different TOF values should be due to their different available Co sites. The 3DOM structure of Co-SA/3DOM-NC can accelerate the mass transfer of reactants and enhance the accessibility of the active sites, leading to superior catalytic performance. However, Co-SA/NC with a microporous structure shows restricted inner mass transfer, resulting in the unavailability of Co sites with low activity.

In addition, Co-free 3DOM-NC with residual Zn shows much lower catalytic activity (10% conversion), indicating that Co is critical to promote the reaction while Zn shows a negligible role in the reaction (Fig. 6d and Table S5†). Co nanoparticles supported on 3DOM-NC and active carbon were also prepared, denoted Co-NP/3DOM-NC and Co-NP/AC, respectively (Fig. S9–S11†). Co-NP/3DOM-NC exhibits moderate activity (24% conversion), while the Co-NP/AC catalyst showed no catalytic activity. These results imply that Co NPs without N coordination cannot effectively promote the transformation of this reaction and CoN_4 should be the active centers for this reaction. Co-NP/3DOM-

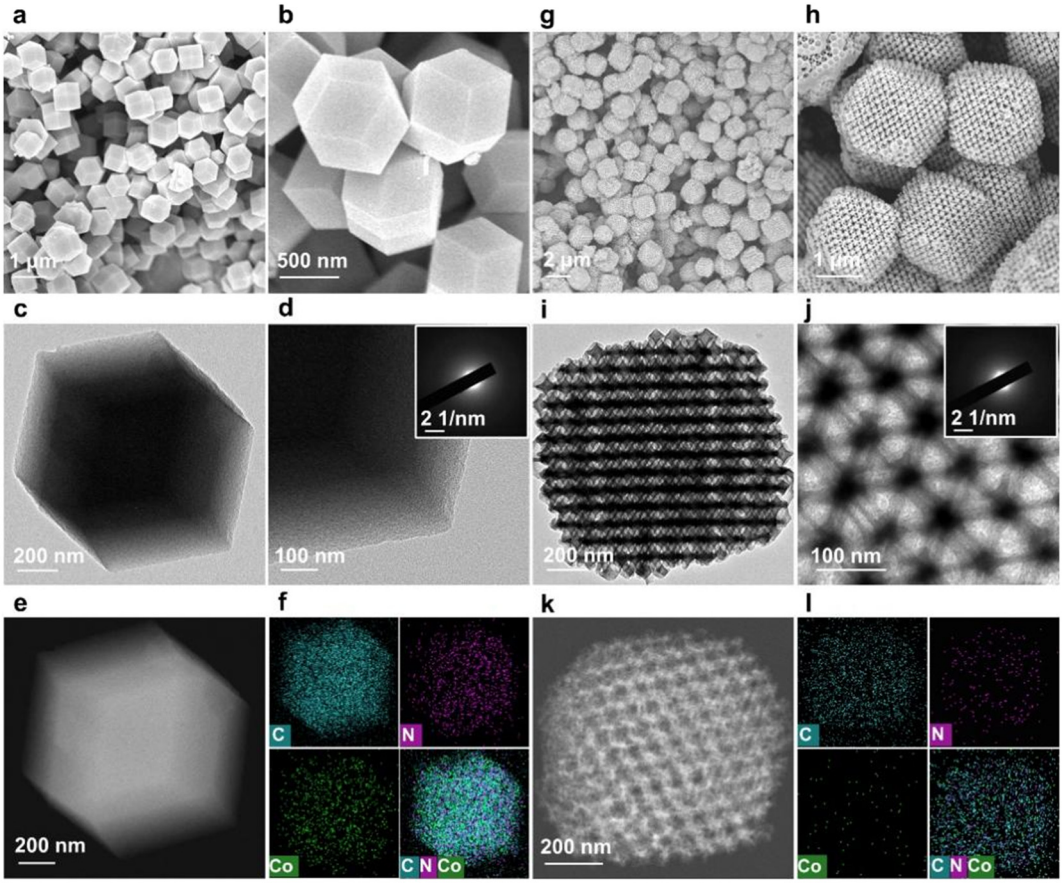

Fig. 5 SEM images of (a and b) Co-SA/NC and (g and h) 3DOM-NC. TEM images of (c and d) Co-SA/NC and (i and j) 3DOM-NC. The insets of (d) and (j) are the SAED patterns of Co-SA/NC and 3DOM-NC, respectively. HAADF-STEM images and corresponding EDS elemental mapping images of (e and f) Co-SA/NC and (k and l) 3DOM-NC.

NC exhibits some activity, which may be due to the existence of CoN_4 sites.[59] The critical role of CoN_4 sites in the catalytic reaction was further verified by thiocyanide (SCN^-) poisoning as SCN^- can strongly bind to the single-atom sites to block the adsorption of the reaction substrate.[60] The FFA conversion decreases from 99% to 21% after the addition of KSCN (Table S5†), confirming that CoN_4 should be the active center for this reaction. Combining the above results, it is demonstrated that the high catalytic activity of Co-SA/3DOM-NC should be attributed to the 3DOM structure with enhanced mass transfer and highly dispersed CoN_4 sites with high intrinsic activity.

To gain more insights into the catalytic mechanism of CoN_4, we have carried out control experiments. The oxidative esterification of FFA was significantly prohibited in the absence of O_2 or the addition of a radical scavenger (*i.e.*, butylated hydroxytoluene) (Table S5†), indicating that the oxidative esterification reaction might involve reactive superoxol ($^{\bullet}O_2^-$) species. The possible reaction mechanism of CoN_4 for the oxidative esterification reaction is proposed as follows.[61,62] O_2 molecules are activated by CoN_4 sites to generate superoxol ($^{\bullet}O_2^-$) species, which can oxidize methanol to methoxy species ($CH_3O^{\bullet}$). Then, the $CH_3O^{\bullet}$ reacts with furfural adsorbed on nitrogen atoms to form hemiacetal species, which is finally converted to methyl 2-furoate through β-H elimination.

Finally, the recyclability of the Co-SA/3DOM-NC material was studied. No remarkable decrease in activity and selectivity were observed even after six cycles (Fig. 6e). The XRD patterns of the reused Co-SA/3DOM-NC only exhibit the diffraction peaks assigned to carbon without Co aggregates (Fig. 7a). High-resolution Co 2p XPS spectra display the same binding energy of Co before and after the reaction (Fig. 7b), indicating the preservation of the chemical state of Co after the reaction. The TEM and HAADF-STEM images of the reused Co-SA/3DOM-NC show that the 3DOM structure was retained and there was no obvious agglomeration of Co (Fig. 7c and e). The aberration-corrected HAADF-STEM image of the reused Co-SA/3DOM-NC shows atomically dispersed Co sites (Fig. 7d), indicating the good stability of the single Co atoms after the reaction. Furthermore, Co, C, and N atoms are uniformly distributed over the whole framework, as confirmed by the EDS elemental mapping images (Fig. 7e). The reaction solution was tested by AAS. The content of Co in the solution is lower than the detection limit (<5 PPb), indicating that the leaching of Co into the solution is negligible. The above results confirm that Co-SA/3DOM-NC

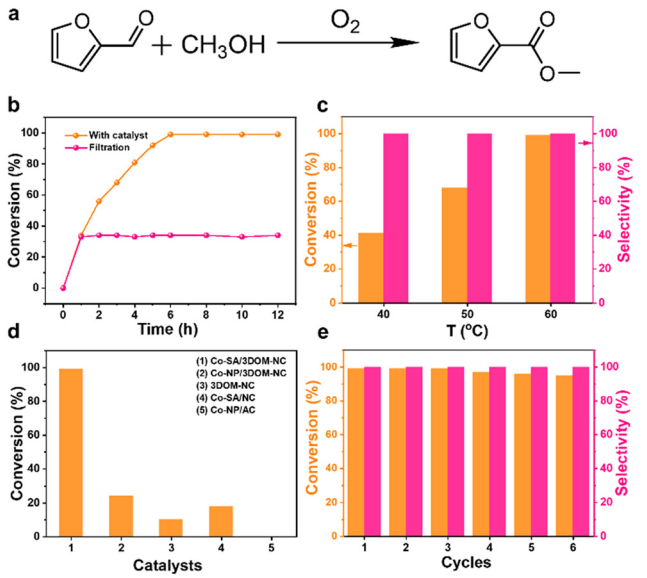

Fig. 6 (a) Catalytic oxidative esterification of FFA to methyl 2-furoate. (b) Activity profiles for the oxidation esterification of FFA over Co-SA/3DOM-NC. (c) The effects of temperature on the FFA conversion and methyl 2-furoate selectivity over Co-SA/3DOM-NC. (d) The comparison of the FFA conversion between Co-SA/3DOM-NC and other catalysts. (e) Reusability tests of Co-SA/3DOM-NC for the oxidative esterification of FFA.

is highly stable in the oxidative esterification reaction of FFA under the optimized reaction conditions.

3 Conclusions

In this study, Co-SA/3DOM-NC with a three-dimensional ordered macropore structure and highly dispersed CoN_4 sites was successfully constructed by two-step pyrolysis of ZnCo-ZIF@PS. The as-prepared Co-SA/3DOM-NC catalyst shows high catalytic activity, selectivity and stability in the oxidative esterification of FFA with methanol to methyl 2-furoate under mild conditions. In addition, the catalyst is highly stable and reusable, without aggregation and leaching of Co after the reaction. This work might provide insights into the development of hierarchically porous support anchored SACs for various catalytic applications.

4 Experimental section

4.1 Materials

The following chemicals were purchased and used without any further purification: cobalt nitrate hexahydrate ($Co(NO_3)_2{\cdot}6H_2O$, 99.95%, Aladdin Industrial Corporation), potassium persulfate ($K_2S_2O_8$, 99 wt%, Tianjin Damao Chemical Co.), ammonium hydroxide ($NH_3{\cdot}H_2O$), styrene (99%, Lingfeng Chemical Co., Ltd.), sodium hydroxide pellets (NaOH, 96%, Guangdong Guanghua Sci-Tech Co., Ltd.), zinc nitrate hexahydrate ($Zn(NO_3)_2{\cdot}6H_2O$, 99%, Shanghai Chemical Reagents), sodium laurylsulfonate (AR, Aladdin Industrial Corporation), cobalt(II) acetylacetonate ($Co(acac)_2$, 97%, Aladdin Industrial Corporation) and 2-methylimidazole (2-MeIM, 98%, Aladdin Industrial Corporation).

4.2 Synthesis of PSs and 3D-PS templates

Uniform PSs with a diameter of 210 nm were prepared by emulsion polymerization.[47] Sodium laurylsulfonate (emulsifying agent, 0.6 g) was dissolved in 360 mL of deionized H_2O followed by addition of 52 mL of styrene. After adding 0.54 g of potassium persulfate, the reaction was performed at 75 °C for 5 h under a nitrogen atmosphere. Monodispersed PSs with sizes of ~210 nm were obtained.

Formation of 3D-PS templates from the monodispersed PSs with a diameter of 210 nm was simply achieved by filtration.[38] The colloidal dispersion was carefully poured onto a filter funnel with three conventional filter papers under vacuum. After 12 h, burly filter cakes were formed, which were further dried at 50 °C overnight to obtain 3D-PS monoliths.

4.3 Synthesis of ZIF-8@PS

The 3D-PS template was immersed into 10 mL of methanol containing 4.08 g of $Zn(NO_3)_2{\cdot}6H_2O$ and 3.38 g of 2-MeIM for 2 h, and was then degassed under vacuum for 30 min to assure the precursor solution entered the voids of the template. The obtained 3D-PS@precursor was transferred to a clean beaker and dried at 50 °C overnight. Afterwards, the dry 3D-PS@precursor was immersed in a mixed solution of $NH_3{\cdot}H_2O/CH_3OH$ (1 : 1 v/v) and then degassed under vacuum for 30 min to ensure the mixed solution was homogeneously permeated. The above solution was left for crystallization for 24 h. ZIF-8@PS was obtained after washing with methanol several times and drying at 50 °C for several hours.

4.4 Synthesis of ZnCo-ZIF@PS

The 3D-PS template was immersed into a 10 mL of methanol solution containing 3.88 g of $Zn(NO_3)_2{\cdot}6H_2O$, 0.2 g of $Co(NO_3)_2{\cdot}6H_2O$, and 3.38 g of 2-methylimidazole for 2 h, and was then degassed under vacuum for 30 min to assure the precursor solution entered the voids of the template. The obtained 3D-PS@precursor was transferred to a clean beaker and dried at 50 °C overnight. Afterwards, the dry 3D-PS@precursor was immersed in a mixed solution of $NH_3{\cdot}H_2O/CH_3OH$ (1 : 1 v/v) and then degassed under vacuum for 30 min to ensure the mixed solution was homogeneously permeated. The above solution was left for complete crystallization for 24 h. ZnCo-ZIF@PS was obtained after washing with methanol several times and drying at 50 °C for several hours.

4.5 Synthesis of Co-SA/3DOM-NC

The as-synthesized ZnCo-ZIF@PS was placed in a tubular furnace and heated to 400 °C with a ramping rate of 5 °C min^{-1} and kept at 400 °C for 5 h in flowing Ar, then to 920 °C with a ramping rate of 5 °C min^{-1} and kept at 920 °C for 3

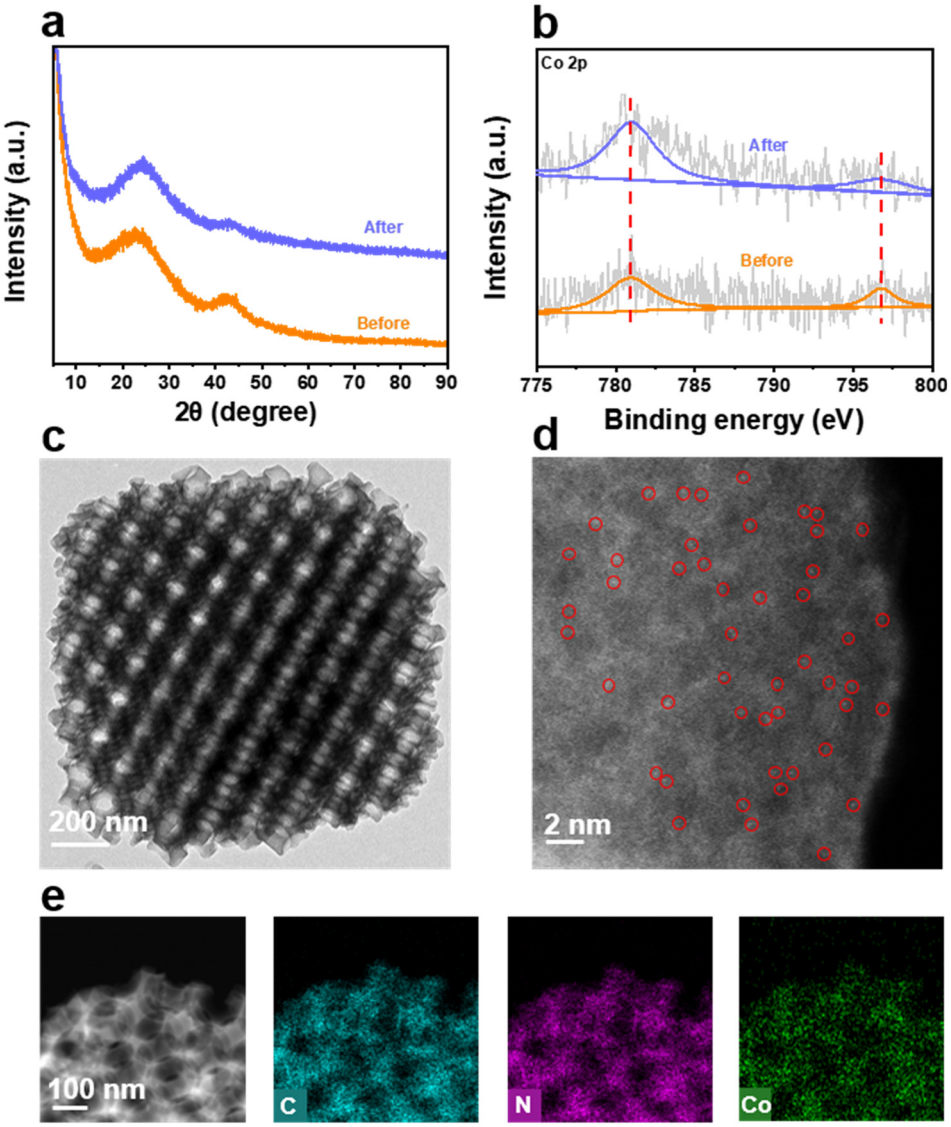

Fig. 7 (a) XRD patterns and (b) high-resolution Co 2p XPS spectra of Co-SA/3DOM-NC before and after the reaction. (c) TEM, (d) aberration-corrected HAADF-STEM, and (e) HAADF-STEM and corresponding EDS elemental mapping images of Co-SA/3DOM-NC after the reaction.

h. The obtained black powders were denoted Co-SA/3DOM-NC.

4.6 Synthesis of C-ZnCo-ZIF

1.0 g of $Zn(CH_3COO)_2{\cdot}2H_2O$ and 0.02 g $Co(NO_3)_2{\cdot}2H_2O$ were dissolved in 20 mL of H_2O (solution A). 12.0 g of 2-MeIm was dissolved in 180 mL of H_2O (solution B). Then, solution B was poured into solution A. After mixing and stirring at room temperature for 24 h, the precipitates were centrifuged and washed with H_2O and MeOH several times and finally dried overnight at 60 °C.

4.7 Synthesis of Co-SA/NC

The as-synthesized C-ZnCo-ZIF was placed in a tubular furnace and heated to 600 °C with a ramping rate of 5 °C min^{-1} and kept at 920 °C for 3 h in flowing Ar. The obtained black powders were denoted Co-SA/NC.

4.8 Synthesis of 3DOM-NC

The as-synthesized ZIF-8@PS was placed in a tubular furnace and heated to 400 °C with a ramping rate of 5 °C min^{-1} and kept at 400 °C for 5 h, then to 920 °C with a ramping rate of 5 °C min^{-1} and kept at 920 °C for 3 h in flowing Ar. The obtained black powders were denoted 3DOM-NC.

4.9 Oxidative esterification of furfural

For a typical catalytic test, furfural (FFA, 0.1 mmol), CH_3OH (1 mL), and a certain amount of catalysts (0.0029 mmol of Co) were added into a Schlenk tube with a magnetic stirrer. The Schlenk tube was evacuated, refilled with 1 bar O_2, and

heated to 60 °C for 6 h under magnetic stirring. After reaction, the reactor was cooled to room temperature. The catalyst was isolated from the solution by centrifugation. The products were analyzed using a GC-MS (Agilent, 7890B GC/5977A MS) equipped with an HP-5 MS capillary column (0.25 mm × 30 m). The influence of temperature was investigated by using the above reaction conditions but using different temperatures.

4.10 Recycling of the catalyst

The recyclability of the catalyst was tested in the oxidative esterification of furfural under the same reaction conditions as described above, except for using the recovered catalyst. Each time, the catalyst was separated from the reaction mixture by centrifugation at the end of the reaction, thoroughly washed with ethyl acetate three times, and then reused directly for the next run.

Author contributions

L. C. and Y. L. conceived the idea and designed the work. W. Y. performed material synthesis, characterization, and catalytic tests. Y. Z. performed TEM measurements. C. H., H. L., F. W., and K. S. helped with characterization. W. Y., L. C., and Y. L. co-wrote the paper. All the authors discussed the results and commented on the manuscript.

Conflicts of interest

The authors declare no conflict of interest.

Acknowledgements

This work was supported by the National Natural Science Foundation of China (No. 21825802, 22138003, and 22108083), the Fundamental Research Funds for the Central Universities (No. 2022ZYGXZR017 and 2022ZYGXZR108), the Foundation of Advanced Catalytic Engineering Research Center of the Ministry of Education (No. 2020AC006), the State Key Laboratory of Pulp and Paper Engineering (No. 2022C04 and 2022ZD05), the Guangdong Pearl River Talents Program (No. 2021ZT09Z109 and 2021QN02C8), the Natural Science Foundation of Guangdong Province (No. 2017A030312005 and 2022A1515012575), the Guangdong Basic and Applied Basic Research Foundation (No. 2021A1515110413), and the Science and Technology Program of Guangzhou (No. 202201010118).

References

1 T. Ennaert, J. V. Aelst, J. Dijkmans, R. D. Clercq, W. Schutyser, M. Dusselier, D. Verboekend and B. F. Sels, Potential and challenges of zeolite chemistry in the catalytic conversion of biomass, *Chem. Soc. Rev.*, 2016, **45**, 584–611.

2 R. Fang, A. Dhakshinamoorthy, Y. Li and H. Garcia, Metal organic frameworks for biomass conversion, *Chem. Soc. Rev.*, 2020, **49**, 3638–3687.

3 S. Zhang, J. Sun, X. Zhang, J. Xin, Q. Miao and J. Wang, Ionic liquid-based green processes for energy production, *Chem. Soc. Rev.*, 2014, **43**, 7838–7869.

4 Y. Yang, W. Zhang, F. Yang, B. Zhou, D. Zeng, N. Zhang, G. Zhao, S. Hao and X. Zhang, Ru nanoparticles dispersed on magnetic yolk-shell nanoarchitectures with Fe_3O_4 core and sulfoacid-containing periodic mesoporous organosilica shell as bifunctional catalysts for direct conversion of cellulose to isosorbide, *Nanoscale*, 2018, **10**, 2199–2206.

5 C. Xu, E. Paone, D. Rodríguez-Padrón, R. Luque and F. Mauriello, Recent catalytic routes for the preparation and the upgrading of biomass derived furfural and 5-hydroxymethylfurfural, *Chem. Soc. Rev.*, 2020, **49**, 4273–4306.

6 N. Li and M.-H. Zong, (Chemo)biocatalytic Upgrading of Biobased Furanic Platforms to Chemicals, Fuels, and Materials: A Comprehensive Review, *ACS Catal.*, 2022, **12**, 10080–10114.

7 P. Sudarsanam, E. Peeters, E. V. Makshina, V. I. Parvulescub and B. F. Sels, Advances in porous and nanoscale catalysts for viable biomass conversion, *Chem. Soc. Rev.*, 2019, **48**, 2366–2421.

8 X. Wu, J. Li, S. Xie, P. Duan, H. Zhang, J. Feng, Q. Zhang, J. Cheng and Y. Wang, Selectivity Control in Photocatalytic Valorization of Biomass-Derived Platform Compounds by Surface Engineering of Titanium Oxide, *Chem*, 2020, **6**, 3038–3053.

9 X. Tong, Z. Liu, L. Yua and Y. Li, A tunable process: catalytic transformation of renewable furfural with aliphatic alcohols in the presence of molecular oxygen, *Chem. Commun.*, 2015, **51**, 3674–3677.

10 C. Ampelli, G. Centi, C. Genovese, G. Papanikolaou, R. Pizzi, S. Perathoner, R.-J. van Putten, K. J. P. Schouten, A. C. Gluhoi and J. C. van der Waa, A Comparative Catalyst Evaluation for the Selective Oxidative Esterification of Furfural, *Top. Catal.*, 2016, **59**, 1659–1667.

11 R. Radhakrishnan, S. Thiripuranthagan, A. Devarajan, S. Kumaravel, E. Erusappan and K. Kannan, Oxidative esterification of furfural by Au nanoparticles supported CMK-3 mesoporous catalysts, *Appl. Catal., A*, 2017, **545**, 33–43.

12 M. Signoretto, F. Menegazzo, L. Contessotto, F. Pinna, M. Manzoli and F. Boccuzzi, Au/ZrO_2: an efficient and reusable catalyst for the oxidative esterification of renewable furfural, *Appl. Catal., B*, 2013, **129**, 287–293.

13 F. Menegazzo, M. Signoretto, F. Pinna, M. Manzoli, V. Aina, G. Cerrat and F. Boccuzzi, Oxidative esterification of renewable furfural on gold-based catalysts: Which is the best support?, *J. Catal.*, 2014, **309**, 241–247.

14 K. Jiang, S. Siahrostami, T. Zheng, Y. Hu, S. Hwang, E. Stavitski, Y. Peng, J. Dynes, M. Gangisetty, D. Su, K. Attenkoferf and H. Wang, Isolated Ni single atoms in graphene nanosheets for high-performance CO_2 reduction, *Energy Environ. Sci.*, 2018, **11**, 893–903.

15 L. Zhang, Y. Jia, G. Gao, X. Yan, N. Chen, J. Chen, M. T. Soo, B. Wood, D. Yang, A. Du and X. Yao, Graphene Defects Trap

Atomic Ni Species for Hydrogen and Oxygen Evolution Reactions, *Chem*, 2017, **4**, 285–297.

16 Y. Han, Y.-G. Wang, W. Chen, R. Xu, L. Zheng, J. Zhang, J. Luo, R.-A. Shen, Y. Zhu, W.-C. Cheong, C. Chen, Q. Peng, D. Wang and Y. Li, Hollow N-Doped Carbon Spheres with Isolated Cobalt Single Atomic Sites: Superior Electrocatalysts for Oxygen Reduction, *J. Am. Chem. Soc.*, 2017, **139**, 17269–17272.

17 J. Yang, W. Liu, M. Xu, X. Liu, H. Qi, L. Zhang, X. Yang, S. Niu, D. Zhou, Y. Liu, Y. Su, J.-F. Li, Z.-Q. Tian, W. Zhou, A. Wang and T. Zhang, *J. Am. Chem. Soc.*, 2021, **143**, 14530–14539.

18 L. Jiao, R. Zhang, G. Wan, W. Yang, X. Wan, H. Zhou, J. Shui, S.-H. Yu and H.-L. Jiang, Nanocasting SiO_2 into metal-organic frameworks imparts dual protection to high-loading Fe single-atom electrocatalysts, *Nat. Commun.*, 2020, **11**, 2831.

19 T. Zhang, X. Han, H. Liu, M. Biset-Peiró, J. Li, X. Zhang, P. Tang, B. Yang, L. Zheng, J. R. Morante and J. Arbiol, Site-Specific Axial Oxygen Coordinated FeN_4 Active Sites for Highly Selective Electroreduction of Carbon Dioxide, *Adv. Funct. Mater.*, 2022, **32**, 2111446.

20 H. Liu, M. Cheng, Y. Liu, J. Wang, G. Zhang, L. Li, L. Du, G. Wang, S. Yang and X. Wang, Single atoms meet metal–organic frameworks: collaborative efforts for efficient photocatalysis, *Energy Environ. Sci.*, 2022, **15**, 3722–3749.

21 Z. Liang, C. Qu, D. Xia, R. Zou and Q. Xu, Atomically Dispersed Metal Sites in MOF-Based Materials for Electrocatalytic and Photocatalytic Energy Conversion, *Angew. Chem., Int. Ed.*, 2018, **57**, 9604–9633.

22 H.-F. Wang, L. Chen, H. Pang, S. Kaskel and Q. Xu, MOF-derived electrocatalysts for oxygen reduction, oxygen evolution and hydrogen evolution reactions, *Chem. Soc. Rev.*, 2020, **49**, 1414–1448.

23 L. Chen, H.-F. Wang, C. Li and Q. Xu, Bimetallic metal-organic frameworks and their derivatives, *Chem. Sci.*, 2020, **11**, 5369–5403.

24 H. Huang, K. Shen, F. Chen and Y. Li, Metal-Organic Frameworks as a Good Platform for the Fabrication of Single-Atom Catalysts, *ACS Catal.*, 2020, **10**, 6579–6586.

25 J. Li, H. Huang, P. Liu, X. Song, D. Mei, Y. Tang, X. Wang and C. Zhong, Metal-organic framework encapsulated single-atom Pt catalysts for efficient photocatalytic hydrogen evolution, *J. Catal.*, 2019, **375**, 351–360.

26 Z. Liang, C. Qu, D. Xia, R. Zou and Q. Xu, Atomically Dispersed Metal Sites in MOF-Based Materials for Electrocatalytic and Photocatalytic Energy Conversion, *Angew. Chem., Int. Ed.*, 2018, **57**, 9604–9633.

27 W. Qu, C. Chen, Z. Tang, H. Wen, L. Hu, D. Xia, S. Tian, H. Zhao, C. He and D. Shu, Progress in metal-organic-framework-based single-atom catalysts for environmental remediation, *Coord. Chem. Rev.*, 2023, **474**, 214855.

28 W. Yang, X. Li, Y. Li, R. Zhu and H. Pang, Applications of Metal–Organic-Framework-Derived Carbon Materials, *Adv. Mater.*, 2019, **31**, 1804740.

29 T. Sun, Y. Li, T. Cui, L. Xu, Y.-G. Wang, W. Chen, P. Zhang, T. Zheng, X. Fu, S. Zhang, Z. Zhang, D. Wang and Y. Li, Engineering of Coordination Environment and Multiscale Structure in Single-Site Copper Catalyst for Superior Electrocatalytic Oxygen Reduction, *Nano Lett.*, 2020, **20**, 6206–6214.

30 T. Zhang, X. Han, H. Liu, M. Biset-Peiró, J. Li, X. Zhang, P. Tang, B. Yang, L. Zheng, J. R. Morante and J. Arbiol, Site-Specific Axial Oxygen Coordinated FeN_4 Active Sites for Highly Selective Electroreduction of Carbon Dioxide, *Adv. Funct. Mater.*, 2022, **32**, 2111446.

31 Y. Zhang, L. Jiao, W. Yang, C. Xie and H.-L. Jiang, Rational Fabrication of Low-Coordinate Single-Atom Ni Electrocatalysts by MOFs for Highly Selective CO_2 Reduction, *Angew. Chem.*, 2021, **60**, 7607–7611.

32 Y. He, Q. Shi, W. Shan, X. Li, A. J. Kropf, E. C. Wegener, J. Wright, S. Karakalos, D. Su, D. A. Cullen, G. Wang, D. J. Myers and G. Wu, Dynamically Unveiling Metal-Nitrogen Coordination during Thermal Activation to Design High-Efficient Atomically Dispersed CoN_4 Active Sites, *Angew. Chem., Int. Ed.*, 2021, **60**, 9516–9526.

33 Y. Ha, B. Fei, X. Yan, H. Xu, Z. Chen, L. Shi, M. Fu, W. Xu and R. Wu, Atomically Dispersed Co-Pyridinic N-C for Superior Oxygen Reduction Reaction, *Adv. Energy Mater.*, 2020, **10**, 2002592.

34 C. Hu, Y. Wang, J. Chen, H.-F. Wang, K. Shen, K. Tang, L. Chen and Y. Li, Main-Group Metal Single-Atomic Regulators in Dual-Metal Catalysts for Enhanced Electrochemical CO_2 Reduction, *Small*, 2022, **18**, 2201391.

35 H. Yang, X. Liu, M. Hao, Y. Xie, X. Wang, H. Tian, G. I. N. Waterhouse, P. E. Kruger, S. G. Telfer and S. Ma, Functionalized Iron-Nitrogen-Carbon Electrocatalyst Provides a Reversible Electron Transfer Platform for Efficient Uranium Extraction from Seawater, *Adv. Mater.*, 2021, **33**, 2106621.

36 Y. Tao, S. W. Zuo, S. Hao Xiao, P. X. Sun, N. W. Li, J. S. Chen, H. B. Zhang and L. Yu, Atomically Dispersed Cu in Zeolitic Imidazolate Framework Nanoflake Array for Dendrite-Free Zn Metal Anode, *Small*, 2022, **18**, 2203231.

37 X. Liu, Y. Xie, M. Hao, Z. Chen, H. Yang, G. I. N. Waterhouse, S. Ma and X. Wang, Highly Efficient Electrocatalytic Uranium Extraction from Seawater over an Amidoxime-Functionalized In-N-C Catalyst, *Adv. Sci.*, 2022, **9**, 2201735.

38 K. Shen, L. Zhang, X. Chen, L. Liu, D. Zhang, Y. Han, J. Chen, J. Long, R. Luque, Y. Li and B. Chen, Ordered macro-microporous metal organic framework single crystals, *Science*, 2018, **359**, 206–210.

39 Z. Zhu, H. Yin, Y. Wang, C.-H. Chuang, L. Xing, M. Dong, Y.-R. Lu, G. Casillas-Garcia, Y. Zheng, S. Chen, Y. Dou, P. Liu, Q. Cheng and H. Zhao, Coexisting Single-Atomic Fe and Ni Sites on Hierarchically Ordered Porous Carbon as a Highly Efficient ORR Electrocatalyst, *Adv. Mater.*, 2020, **32**, 2004670.

40 M. Qiao, Y. Wang, Q. Wang, G. Hu, X. Mamat, S. Zhang and S. Wang, Hierarchically Ordered Porous Carbon with

Atomically Dispersed FeN_4 for Ultra-efficient Oxygen Reduction Reaction in PEMFC, *Angew. Chem., Int. Ed.*, 2020, **59**, 2688–2694.

41 C. Zhao, G.-L. Xu, Z. Yu, L. Zhang, I. Hwang, Y.-X. Mo, Y. Ren, L. Cheng, C.-J. Sun, Y. Ren, X. Zuo, J.-T. Li, S.-G. Sun, K. Amine and T. Zhao, A high-energy and long-cycling lithium–sulfur pouch cell via a macroporous catalytic cathode with double-end binding sites, *Nat. Nanotechnol.*, 2021, **16**, 166–173.

42 X. Peng, L. Chen and Y. Li, Ordered macroporous MOF-based materials for catalysis, *Mol. Catal.*, 2022, **529**, 11256.

43 J. Zou, C. Chen, Y. Chen, Y. Zhu, Q. Cheng, L. Zou, Z. Zou and H. Yang, Facile Steam-Etching Approach to Increase the Active Site Density of an Ordered Porous Fe–N–C Catalyst to Boost Oxygen Reduction Reaction, *ACS Catal.*, 2022, **12**, 4517–4525.

44 Q.-X. Li, D.-H. Si, W. Lin, Y.-B. Wang, H.-J. Zhu, Y.-B. Huang and R. Cao, Highly efficient electroreduction of CO_2 by defect single-atomic Ni-N_3 sites anchored on ordered micro-macroporous carbons, *Sci. China: Chem.*, 2022, **65**, 1584–1593.

45 X. Zhang, X. Han, Z. Jiang, J. Xu, L. Chen, Y. Xue, A. Nie, Z. Xie, Q. Kuang and L. Zheng, Atomically dispersed hierarchically ordered porous Fe–N–C electrocatalyst for high performance electrocatalytic oxygen reduction in Zn-Air battery, *Nano Energy*, 2020, **71**, 104547.

46 T. Sun, S. Zhao, W. Chen, D. Zhai, J. Dong, Y. Wang, S. Zhang, A. Han, L. Gu, R. Yu, X. Wen, H. Ren, L. Xu, C. Chen, Q. Peng, D. Wang and Y. Li, Single-atomic cobalt sites embedded in hierarchically ordered porous nitrogen-doped carbon as a superior bifunctional electrocatalyst, *Proc. Natl. Acad. Sci. U. S. A.*, 2018, **115**, 12692–12697.

47 M. H. Sun, J. Zhou, Z. Y. Hu, L. H. Chen, L. Y. Li, Y. D. Wang and Z. K. Xie, Hierarchical Zeolite Single-Crystal Reactor for Excellent Catalytic Efficiency, *Matter*, 2020, **3**, 1226–1245.

48 W. Liu, L. Zhang, W. Yan, X. Liu, X. Yang, S. Miao, W. Wang, A. Wang and T. Zhang, Single-atom dispersed Co-N-C catalyst: structure identification and performance for hydrogenative coupling of nitroarenes, *Chem. Sci.*, 2016, **7**, 5758–5764.

49 L. Li, C. Tang, Y. Zheng, B. Xia, X. Zhou, H. Xu and S.-Z. Qiao, Tailoring Selectivity of Electrochemical Hydrogen Peroxide Generation by Tunable Pyrrolic-Nitrogen-Carbon, *Adv. Energy Mater.*, 2020, **10**, 2000789.

50 J. Ding, D. Guo, A. Hu, X. Yang, K. Shen, L. Chen and Y. Li, Resisting metal aggregation in pyrolysis of MOFs towards highdensity metal nanocatalysts for efficient hydrazine assisted hydrogen production, *Nano Res.*, 2022, DOI: **10.1007/s12274-022-4777-5**.

51 H. Li, X. Chen, J. Chen, K. Shen and Y. Li, Hierarchically porous Fe,N-doped carbon nanorods derived from 1D Fe-doped MOFs as highly efficient oxygen reduction electrocatalysts in both alkaline and acidic media, *Nanoscale*, 2021, **13**, 10500–10508.

52 N. Zhou, Y. Du, C. Wang and R. Chen, Facile synthesis of hierarchically porous carbons by controlling the initial oxygen concentration in-situ carbonization of ZIF-8 for efficient water treatment, *Chin. J. Chem. Eng.*, 2018, **26**, 2523–2530.

53 J. Ding, H.-F. Wang, X. Yang, W. Ju, K. Shen, L. Chen and Y. Li, A Janus heteroatom-doped carbon electrocatalyst for hydrazine oxidation, *Natl. Sci. Rev.*, 2022, DOI: **10.1093/nsr/nwac231**.

54 W. Yao, J. Chen, Y. Wang, R. Fang, Z. Qin, X. Yang, L. Chen and Y. Li, Nitrogen-Doped Carbon Composites with Ordered Macropores and Hollow Walls, *Angew. Chem., Int. Ed.*, 2021, **60**, 23729–23734.

55 Y. Zhao, Y. Guo, X. F. Lu, D. Luan, X. Gu and X. W. Lou, Exposing Single Ni Atoms in Hollow S/N-Doped Carbon Macroporous Fibers for Highly Efficient Electrochemical Oxygen Evolution, *Adv. Mater.*, 2022, **34**, 2203442.

56 F. Liu, L. Shi, X. Lin, D. Yu, C. Zhang, R. Xu, D. Liu, J. Qiu and L. Dai, Site-density engineering of single-atomic iron catalysts for high-performance proton exchange membrane fuel cells, *Appl. Catal., B*, 2022, **302**, 120860.

57 L. Chen, L. Zhang, Z. Chen, H. Liu, R. Luque and Y. Li, A covalent organic framework-based route to the in situ encapsulation of metal nanoparticles in N-rich hollow carbon spheres, *Chem. Sci.*, 2016, **7**, 6015–6020.

58 X. Hu, G. Luo, Q. Zhao, D. Wu, T. Yang, J. Wen, R. Wang, C. Xu and N. Hu, Ru Single Atoms on N-Doped Carbon by Spatial Confifinement and Ionic Substitution Strategies for High-Performance Li–O_2 Batteries, *J. Am. Chem. Soc.*, 2020, **142**, 16776–16786.

59 X. Qiu, J. Chen, X. Zou, R. Fang, L. Chen, Z. Chen, K. Shen and Y. Li, Encapsulation of C–N-decorated metal sub-nanoclusters/single atoms into a metal-organic framework for highly efficient catalysis, *Chem. Sci.*, 2018, **9**, 8962–8968.

60 R. V. Jagadeesh, K. Murugesan, A. S. Alshammari, H. Neumann, M. M. Pohl, J. Radnik and M. Beller, MOF-derived cobalt nanoparticles catalyze a general synthesis of amines, *Science*, 2017, **358**, 326–332.

61 D. Yin, Y. Zheng, L. Yang, S. Li, D. Zhu, Y. Guo, C. Zuo, Y. Li, H. Huang and M. Wang, Oxidative esterifification of renewable furfural on cobalt dispersed on ordered porous nitrogen doped carbon, *RSC Adv.*, 2021, **11**, 3280–3287.

62 Y. Tian, Y. Li, Y. Zheng, M. Wang, C. Zuo, H. Huang, D. Yin, Z. Fu, J. Tan and Z. Zhou, Nano-Au/$MCeO_x$ Catalysts for the Direct Oxidative Esterification of Methylacrolein to Methyl Esters, *Ind. Eng. Chem. Res.*, 2019, **58**, 19397–19405.